High-Temperature CO_2 Separation from Flue Gas Using Ceramic Membranes: Experimental Insights and Artificial Neural Network Modeling

Mohammod H. Rahman[1], Abdelrahman G. Gadalla[1,4], Karim Kriaa[1,3], Saad A. Aljlil[2], Abdullah K. Alshamari[2], AbdulAziz A. AlGhamdi[1], H. E. Fawaz[5*]

[1]*Chemical Engineering Department, Imam Mohammad Ibn Saud Islamic University, Riyadh11432, Saudi Arabia.*
[2]*National Center for Water Technologies, King Abdulaziz City for Science & Technology, Riyadh 11442, Saudi Arabia.*
[3]*Research and Technology Center of Energy, Technoparc borje cedria, BP 095 Hammam Lif, Tunisia.*
[4]*Department of Chemical engineering and pilot plant, National Research Centre, Giza 12622, Egypt.*
[5]*Department of Mechanical Engineering, National Research Centre, Giza 12622, Egypt.*
Email: hanyfawaz79@gmail.com

Abstract: The effective capturing of carbon dioxide (CO_2) from flue gases represents an important environmental and economic challenge, where such emissions are considered a major contributor to global climate issue. Traditional capturing techniques such as amine scrubbing are energy-intensive with high cost, due to the necessity of cooling high temperature flue gases before the separation process. In this study, we investigated the utilization of ceramic membranes fabricated from Saudi red clay which considered an available, cost-effective local material as a sustainable solution for high-temperature CO_2 capture. The research evaluates separation efficiency under high temperatures and different pressure values, which enable direct CO_2 capturing from hot flue streams without precooling processes. Experimental results demonstrate the membranes efficacy in separating CO_2 from flue gas, in which the presence of iron oxide (Fe_2O_3) constituents in the clay enhancing capture efficiency through weak chemisorption. In addition, the membranes showed robust structural integrity and consistent performance under high temperature conditions, compared to polymeric membranes that degrade thermally and offer advantages over metal-organic framework-enhanced ceramics, which incur higher costs and lower thermal tolerance. An ANN model is constructed to estimate the membrane performance (CO2 concentration (%) in permeate) using results obtained from the present experimental results and utilizing pressure and temperature as ANN input parameters. The process of training incorporates the analysis of the loss function on training and validation data for controlling the weights and biases using backpropagation while feed forward propagate the selected input parameters. A total of 8 hidden layers consisting of 12 neurons each has been used in constructing the ANN, and training process is optimized using the ADAM algorithm to minimize the loss function. The Final layer uses the linear activation function while all the hidden layers use the rectified Linear Units Activation function (ReLU). The ANN model demonstrates excellent predictive performance, yielding values close to 1 for R2 and r, along with extremely low values for MSE, MAPE, MSLE, and log-cosh loss (0.00033, 0.146%, $4.1\times10^{-}6$, 0.00016 respectively), demonstrating the ANN model's high predictive accuracy.

Keywords: CO_2 Separation; Artificial neural network; Multilayer perceptron; Backpropagation algorithm; ADAM optimizer

1. Introduction

The worldwide effort to manage climate change requires the global community to lower carbon dioxide (CO_2) emissions which reached 36.8 billion metric tons during 2023 [1]. Power generation leads to most emissions at 65% and remains responsible for the continued growth of CO_2 emissions [1]. The combustion process at coal- and gas-fired power plants produces flue gas which includes 10–15% CO_2 mixtures with N_2 and O_2 and water vapor combined with minor amounts of SO_2 and NOx at temperatures ranging from 100°C to 150°C [2]. The combination of weak CO_2 concentration and high temperature along with corrosive trace elements makes it difficult to separate CO_2 in industrial processes requiring efficient and resilient separation technologies [2]. At present international organizations like the Paris Agreement work to achieve the 1.5°C global warming limit while demanding that CO_2 emissions need to decrease by 45% compared to 2010 levels until 2030 [1]. The challenges of current technologies to achieve these targets demonstrate the necessity for industrial-specific innovative solutions. Amine-based scrubbing represents the benchmark for traditional CO_2 capture by achieving greater than 90% removal efficiency from flue gas based on reports [3]. The combination of CO_2 and monoethanolamine (MEA) results in carbamate formation followed by CO_2 release upon heating the substance to regenerate the MEA solvent [3]. The amine scrubbing approach demonstrates excellent operation results but encounters major operational problems. Solutions degrade beyond 120°C thus requiring extensive cooling of flue gas to keep temperatures between 40–60°C before capture [3]. Regeneration of solvents for CO_2 capture requires 3.5–4.0 GJ thermal energy per ton of captured CO_2 thus decreasing power plant effectiveness and raising operational expenses [3, 15]. The operation of the process generates environmental issues because it requires disposal of degraded solvents while volatile organic compounds have potential for release during operation [3].

Research about alternative solutions continues because of operational challenges linked to both elevated temperatures and lower energy costs together with reduced environmental impact. Membrane-based separation functions as an attractive method which utilizes gas permeability disparities to extract CO_2 without chemical solvent use [4]. Membrane systems differ from amine scrubbing because they omit both cooling and regenerative requirements thereby delivering simplified operations and reduced energy requirements [4]. Polyimide-based polymeric membranes stand as prime candidates for CO_2 separation studies because they provide flexible operation with low production expenses [6]. Polymeric membranes lose their functionality when the operating temperature surpasses 280°C because of thermal degradation and experience deteriorating selectivity due to CO_2-induced plasticization throughout the operation duration [6, 8]. Harsh conditions present no challenge for ceramic membranes to handle. The applications of ceramic membranes under high-temperature flue gas treatment become possible because of their 900–1000°C thermal stability and chemical resistance to corrosive gases alongside rigid structures which avoid plasticization. The membrane porosity can be adjusted to enhance gas transport through two mechanisms which are Knudsen diffusion and molecular sieving [9]. The unique properties of ceramic membranes make them an appropriate technology for application in power plant exhaust streams without requiring stream cooling. The development of ceramic membranes received an enhancement through the integration of metal-organic frameworks (MOFs) and zeolites to create mixed-matrix membranes (MMMs) which exhibit CO_2/N_2 selectivity from 4 to 10 at temperatures under 80°C [7, 17]. The research conducted by Li et al. [7] exhibited high CO_2 selectivity in MOF-doped ceramics despite the study's challenging synthesis methods and expensive production hurdles [7]. The testing of these meters usually ends at 100°C which creates doubts about their actual operational abilities when exposed to real-world flue gas conditions [8, 18].

Researchers developed a membrane from sustainable local Saudi red clay material that contains 47.63% SiO_2 and 24.03% Al_2O_3 and 9.57% Fe_2O_3 [5]. Saudi Arabia has an abundant supply of red clay for membrane production because the material costs less than alumina membranes ($5 to $10 per square meter compared to $50 to $100 per square meter [16]). Due to the presence of Fe_2O_3 in the structure the membrane shows enhanced CO_2 capture ability through weak chemisorption mechanisms caused by CO_2 quadrupole interaction with Lewis acid sites of Fe_2O_3 [10, 20]. Selectivity receives an improvement through membrane testing at reduced temperatures which establishes the membrane as superior compared to regular ceramic materials. Available research shows that scientists do not comprehend how ceramic membranes behave when exposed to high temperatures using actual flue gas constituents. The studies conducted by Gude et al. [4] demonstrate that ceramic membranes remain thermally stable until 1000°C but provide minimal CO_2 data beyond 120°C [4]. The research by Li et al. [7] worked below

80°C temperatures yet Chen et al. [18] examined melt-down conditions at 800°C without separating CO_2 [18]. The temperatures achieved by flue gases surpass 120°C so that capture operations require heat removal while using amine-based systems to reduce power generation by 15–20% [15]. The research fills this knowledge gap through testing of the red clay-based membrane at temperatures from 60 to 140 degrees Celsius and pressures from 40 to 80 pounds per square inch (psi) using synthetic power plant emissions with CO_2 at 11.9% and O_2 at 2.5% and N_2 at 75.1% and CH_4 at 0.5%. The membrane operation at these conditions would eliminate cooling procedures while providing an efficient commercial deployment solution. The research uses an artificial neural network (ANN) model combined with experimental results to make predictions for membrane performance.

The neural network technology effectively models complex non-linear data relationships between CO_2 permeation and temperature and pressure variables beyond the limits of traditional empirical Modeling [13]. Research data was used to train the ANN model by taking temperature and pressure values as inputs for CO_2 separation behaviour predictions [13]. A methodology based on ANNs enhances the work conducted by Sema et al. [13] during CO_2 capture process Modeling and expands its application to membrane systems operating at elevated temperatures. The model provides forecasting capabilities which allow engineers to make real-time changes that enhance operation performance during industrial process adjustments. The expanded initial section provides foundation for a comprehensive study on sustainable ceramic membrane separation of CO_2. The research focuses on improving carbon capture methods through a combination of Saudi red clay exploitation combined with high-temperature solutions and modern Modeling techniques. A thorough evaluation of this technology's potential for fossil fuel-based power generation emission reduction follows through sections describing membrane fabrication and experimental observations and ANN prediction analysis.

2. Materials and Methods

2.1. Membrane Fabrication and Characterization

The membrane sample was prepared from Saudi red clay at 91.5 wt% with tetraethyl orthosilicate at 1.5 wt% together with sodium alginate as the 2 wt% binder and ammonia functioning at 5 wt% as the catalyst. A manufacturing sequence included milling the clay particles to sub-125 μm and producing 10 mm diameter cylindrical membranes with 2 mm thickness before a three-day drying period. These membranes underwent a two-stage sintering process combining burnout from 25 to 500 ºC at one degree Celsius per minute followed by densification from 500 to 1000 degrees Celsius at 2 degrees Celsius per minute for three hours. The 0.8–1.2 μm pores of the membrane structure became visible through SEM (JEOL JSM-6360LV) whereas EDS (energy-dispersive X-ray spectroscopy) established Si, Al, and Fe as major components according to Figure 1.

2.2. Experimental Setup

The custom-made membrane module functioned as part of an Agilent 7890B gas chromatograph. Each test lasting 2 hours maintained stable conditions where the flue gas sample operated at 40–80 psi and 21–140°C (see Figure 2 for the experimental setup which included the heater, gas supply and membrane separation cell and gas chromatograph).

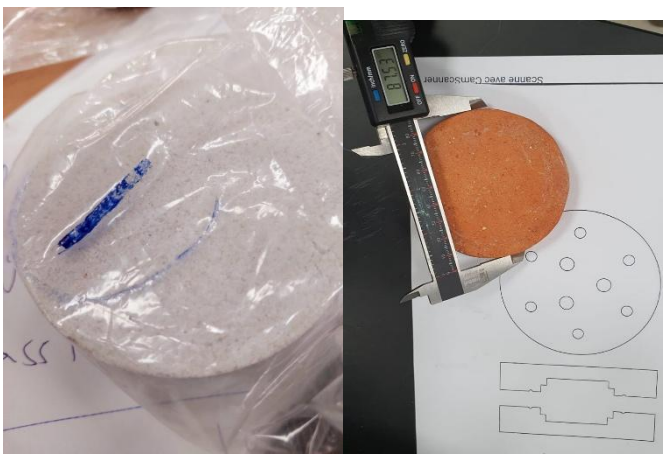

Fig. 1. Red clay and silica-based ceramic membrane samples.

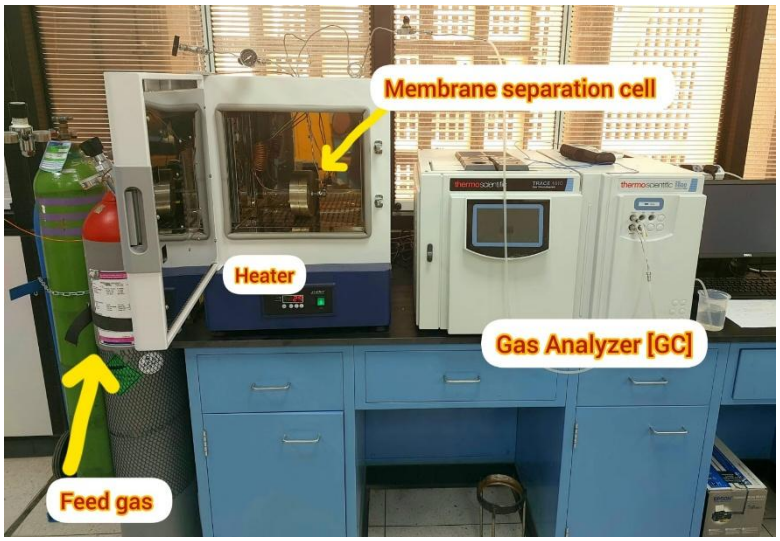

Fig. 2. Experimental setup including heater, gas supply, membrane separation cell, and gas chromatograph.

3. Artificial Neural Network Architecture

An artificial neural network (ANN) operates in this study to make prediction of CO_2 separation performance through different temperature and pressure conditions. This network architecture contains an input layer followed by repetitions of hidden (ReLU) activation function layers then an output layer with linear activation. During training the backpropagation algorithm utilizes ADAM optimizer to execute the process. The proposed model uses mean squared error (MSE) as its loss function to measure performance during evaluation. Figure 3 shows the schematic diagram of the proposed ANN model with a detailed description provided in this section.

3.1 Input Layer

The initial step for input data into the ANN model takes place through its input layer which accepts independent variables T and P that strongly affect CO_2 separation results. Every input variable receives a separate neuron in the input layer of the ANN. The mathematical representation of the input vector appears as:

$$X = [T, P]^T \quad (1)$$

where T and P are normalized to a standard range (between 0 and 1) using min-max scaling or standardization to ensure stable learning.

3.2 Hidden Layers

The hidden layers perform nonlinear transformations on the input data to learn complex relationships between temperature, pressure, and CO_2 separation performance. Each neuron in a hidden layer receives weighted inputs from the previous layer and applies an activation function to introduce nonlinearity into the model. The ReLU activation function is used for all hidden neurons and is mathematically defined as:

$$f(z) = \max(0, z) \quad (2)$$

where z is the weighted sum of inputs plus the bias term, given by:

$$z_j^{(m)} = \sum_{i=1}^{n^{(m-1)}} w_{ij}^{(m)} a_i^{(m-1)} + b_j^{(m)} \quad (3)$$

where $w_{ij}^{(m)}$ represents the weight connecting the ith neuron in layer (m−1) to the jth neuron in layer m, $b_j^{(m)}$is the bias term, and $a_i^{(m-1)}$ is the activation of the ith neuron from the previous layer. The output of each hidden neuron is then computed as:

$$a_j^{(m)} = f\left(z_j^{(m)}\right) = \max\left(0, z_j^{(m)}\right) \quad (4)$$

The ReLU function is computationally efficient and helps mitigate the vanishing gradient problem, making it suitable for deep learning models.

3.3 Output Layer

The output layer consists of a single neuron that predicts the CO_2 separation performance. Unlike the hidden layers, the output neuron employs a linear activation function, allowing the ANN to model

continuous values without any transformation. The output is computed as:

$$\hat{y} = \sum_{i=1}^{n^{(L-1)}} w_i^{(L)} a_i^{(L-1)} + b^{(L)} \quad (5)$$

where $w_i^{(L)}$ and $b^{(L)}$ denote the weights and bias of the output neuron, and $a_i^{(L-1)}$ represents the activation from the final hidden layer.

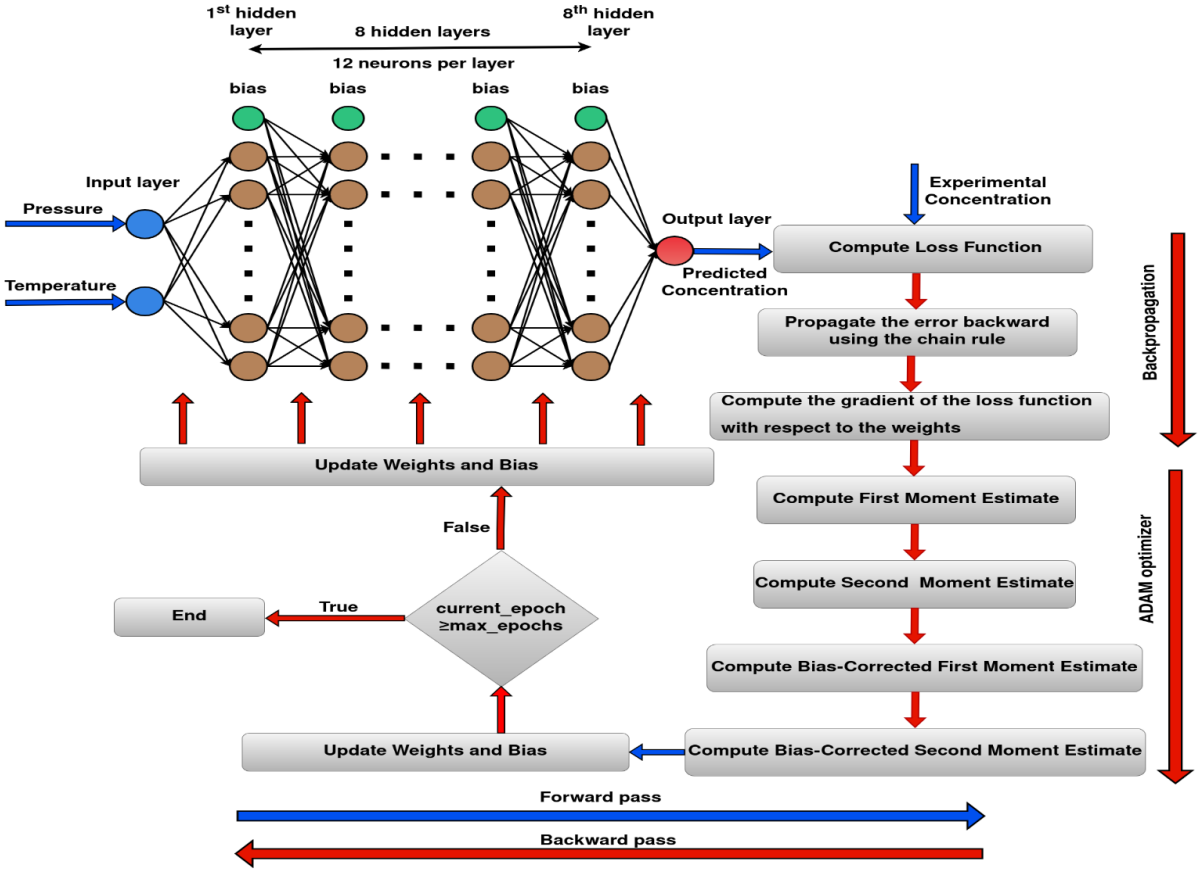

Fig. 3. Schematic diagram of the present ANN model architecture.

3.4 Backpropagation algorithm

The backpropagation algorithm is used to minimize the difference between the predicted ($\hat{y}$) and actual (y) values by iteratively updating the network's weights and biases. The process begins with the computation of the loss function, which in this study is the mean squared error (MSE), defined as:

$$J = \frac{1}{N}\sum_{i=1}^{N}(y_i - \hat{y}_i)^2 \quad (6)$$

where N represents the number of training samples. The gradients of the loss function with respect to the network parameters are computed using the chain rule, propagating errors backward from the output layer to the input layer.

For each weight in layer m, the gradient of the loss function is computed as:

$$\frac{\partial J}{\partial w_{ij}^{(m)}} = \delta_j^{(m)} a_i^{(m-1)} \quad (7)$$

where $\delta_j^{(m)}$ is the error term at neuron j in layer m, defined recursively as:

$$\delta_j^{(m)} = \frac{\partial J}{\partial a_j^{(m)}} \acute{f}\left(z_j^{(m)}\right) \quad (8)$$

For the output layer, the error term is:

$$\delta^{(L)} = \frac{\partial J}{\partial \hat{y}} = 2(\hat{y} - y) \quad (9)$$

For hidden layers, the error term is propagated backward as:

$$\delta^{(m)} = \left(W^{(m+1)}\right)^T \delta^{(m+1)} \odot \acute{f}\left(z^{(m)}\right) \quad (10)$$

where $\odot$ denotes the element-wise product and $\acute{f}\left(z^{(m)}\right)$ is the derivative of the ReLU function:

$$\acute{f}(z) = 1, \text{if} z > 0 \text{ and } \acute{f}(z) = 0, \text{otherwise} \quad (11)$$

Computed gradients are used to update the network parameters using an optimization algorithm.

3.5 ADAM Optimizer

To enhance the convergence speed and stability of the ANN, the Adaptive Moment Estimation (ADAM) optimizer is employed. ADAM combines the advantages of momentum-based and adaptive learning rate methods. The weight update rule for ADAM is given by:

$$m_t = \beta_1 m_{t-1} + (1-\beta_1) g_t \quad (12)$$

$$\upsilon_t = \beta_2 \upsilon_{t-1} + (1-\beta_2) g_t^2 \quad (13)$$

$$\hat{m}_t = \frac{m_t}{1-\beta_1^t}, \hat{\upsilon}_t = \frac{\upsilon_t}{1-\beta_2^t} \quad (14)$$

$$w_t = w_{t-1} - \frac{\eta \hat{m}_t}{\sqrt{\hat{\upsilon}_t}+\epsilon} \quad (15)$$

where g_t is the gradient at iteration t, m_t and υ_t are the first and second moment estimates, respectively, $\beta_1$and β_2 are hyperparameters (typically $\beta_1 = 0.9$ and $\beta_2 = 0.999$), η is the learning rate, and $\epsilon$is a small constant to prevent division by zero. ADAM dynamically adjusts the learning rate for each parameter, leading to more efficient training and reduced sensitivity to hyperparameter selection.

4. Performance loss and evaluating metrics

The model prediction accuracy is tested using loss metrics, which include mean squared error (MSE), mean absolute percentage error (MAPE), mean squared logarithmic error (MSLE), and log cosh loss, and evaluating metrics, which consist of Pearson correlation coefficient (r) and coefficient of determination (R^2).

The MSE evaluates the average squared difference between the predicted and actual values. It presents a measure of how well the model's predictions match the actual values. MSE is continuous and differentiable, making it suitable for optimization algorithms employed in learning models of training machine. Many optimization algorithms, such as gradient descent, rely on the ability to compute gradients, which MSE facilitates. MSE is a loss function of the present model and calculated according to Eq. 6.

In addition, MAPE is a measure of the prediction accuracy of a forecasting method. MAPE is scale-independent, meaning it is not affected by the data scale. This makes it useful for comparing the accomplished accuracy of models across different datasets. MAPE can be estimated using the following formula:

$$\text{MAPE} = \frac{1}{N}\sum_{i=1}^{N}\left|\frac{y_i - \hat{y}_i}{y_i}\right| \text{x}100\% \quad (16)$$

MSLE measures the mean of the squared logarithmic difference of the actual and estimated values. MSLE scales the errors logarithmically, making it less sensitive to extreme values and providing a more balanced evaluation. The formula for MSLE is as below:

$$\text{MSLE} = \frac{1}{N}\sum_{i=1}^{N}\left(\log(y_i+1) - \log(\hat{y}_i+1)\right)^2 \quad (17)$$

Log-cosh loss is a smooth approximation to the tanh function and is often used in regression tasks. One of the key preference of log-cosh loss is its robustness to the outliers. Log-cosh loss penalizes large errors less severely compared to MSE, making it more resilient to outliers. The formula for log-cosh loss is:

$$\log - \cosh - \text{loss} = \sum_{i=1}^{N}\log\left(\cosh(y_i - \hat{y}_i)\right) \quad (18)$$

The direction and strength of a linear relationship between two variables are measured by the Pearson correlation coefficient (r). A perfect positive linear relationship, no linear relationship, and perfect negative linear relationship are represented by 1, 0, and -1, respectively. The r between two variables, y, and $\hat{y}$, with N data points, is calculated using the following formula:

$$r = \frac{\sum_{i=1}^{N}(y_i-\bar{y})(\hat{y}_i-\bar{\hat{y}})}{\sqrt{\sum_{i=1}^{N}(y_i-\bar{y})^2 \sum_{i=1}^{N}(\hat{y}_i-\bar{\hat{y}})^2}} \quad (19)$$

where y_i is the actual value, $\hat{y}_i$ is the predicted value, N is a number of data points, $\bar{y}$ and $\bar{\hat{y}}$ are the means of y and $\hat{y}$, respectively.

The coefficient of determination, denoted by R^2, signifies the fraction of the variance in the dependent variable that can be anticipated from the independent variable. It serves as an assessment of how accurately the regression model conforms to the actual data points. The range of values for R^2 spans from 0 to 1, with one indicating a perfect fit. The formula for R^2 is:

$$R^2 = 1 - \frac{SS_{res}}{SS_{tot}} \quad (20)$$

where the Sum of Squared Residuals (SS_{res}) is the summation of the squared differences between the actual and predicted values.

$$SS_{res} = \sum_{i=1}^{N}(y_i - \hat{y}_i)^2 \quad (21)$$

As well, the total Sum of Squares (SS_{tot}) is the total sum of squares of actual values from its mean.

$$SS_{tot} = \sum_{i=1}^{N}(y_i - \bar{y})^2 \quad (22)$$

5. Results and Discussion

5.1. Temperature Effects on CO_2 Permeation and Selectivity

The concentration of CO_2 in permeation decreased from 7.90% at 60°C to 2.21% at 140°C when operating at 60 psi, while the retentate CO_2 increased from 6.3% to 8.1% based on the provided data in Table 1. At each temperature level CO_2 permeation decreases as the temperature increases because of these two primary mechanisms.

- Thermal Sintering and Pore Dynamics: The pore dimensions of sintering ceramics at elevated temperatures result in reduced openings that mainly impede CO_2 molecules (3.3 Å diameter) compared to N_2 (3.64 Å) and O_2 (3.46 Å) penetration [9]. Rigid ceramic membranes demonstrate temperature-independent CO_2 solubility because the plasticization effect observed in polymeric membranes does not occur in these materials thus, they prefer smaller gases as temperature rises. Research by Chen et al. [18] confirmed that alumina ceramics experienced comparable pore shrinkage at 800°C even though their study did not provide data specific to CO_2.
- Adsorption Dynamics and Fe_2O_3 Influence: The incorporation of 9.57% Fe_2O_3 in the membrane supports CO_2 adsorption via weak chemisorption because Fe_2O_3 Lewis acid sites bind with CO_2's quadrupole moment as reported in [10]. The adsorption process for CO_2 becomes exothermic with temperature hence reducing the amount of time CO_2 stays inside the membrane and lowering its permeance compared to N_2. The selectivity behavior of Fe_2O_3 shows temperature-dependent characteristics which do not appear in traditional ceramics because the oxide material introduces distinct adsorption properties that developers might optimize through altering surface features [11, 20]. Fe_2O_3-doped zeolites at 25–80°C display improved CO_2 adsorption performance according to Yang et al. [20] yet more research is required to examine these effects at 140°C.

The CO_2/N_2 selectivity decreased from 1.8 at 60°C to 0.7 at 140°C as temperature continued to rise which led to increased N_2 permeation. MOF-enriched ceramics show higher CO_2/N_2 selectivity (α_CO_2/N_2 = 4–10) but only affect below 80°C [17] contrary to this material. Our membrane exhibits moderate selectivity but operates effectively at 140°C without experiencing any degradation which makes it suitable for direct flue gas applications while allowing skip of the cooling procedures amine systems need [3]. Our research differs from Gude et al.'s ceramic structure by providing essential high-temperature separation behaviour data even though their materials can operate at temperatures exceeding 1000°C [4]. Our membrane exhibits excellent thermal stability through operating at 140°C because it exceeds carbon molecular sieve membranes' limits of <300°C with its good performance of 100 for α_CO_2/N_2 selectivity [22] as shown in Figure 4 using gas chromatography analysis at 60°C and 60 psi.

5.2. Pressure Effects and Gas Transport Mechanisms

The data showed CO_2 permeation enhanced by 160% from 4.22% to 10.96% throughout the rise in pressure from 40 psi to 80 psi at a constant temperature of 60°C because of elevated partial pressure gradient (Figures 5-8). Research by Zhang et al. [13] at 100°C matches the solution-diffusion model which states that flux directly correlates with driving force ($P = J/\Delta p$) [12]. The longevity of pressure sensitivity even at temperatures up to 140°C allows the membrane to operate effectively in industrial conditions which involve changing gas pressures. The rigid structure of membrane pores shields it from plasticization like polymeric membranes experience under elevated CO_2 pressures which helps to sustain consistent performance [8].

The CO_2 transport function of Fe_2O_3 adsorbents is connected to weak chemisorptive processes according to Yang [10]. The membrane exhibits better CO_2 permeation under low temperatures because adsorption strength becomes more pronounced. investigations for in situ spectroscopy could theoretically measure this interaction because the results may develop improved selectivity in Fe_2O_3-doped membrane designs [20]. The results under real flue gas conditions with moisture and sulfur dioxide will confirm their competitive interaction with CO_2-Fe_2O_3 bonds because tests currently exclude these components [11, 23]. Researchers from Ribeiro et al. [11] discovered that zeolite membranes experienced a 30% decrease

in CO_2 selectivity under conditions of humidity which highlights the necessity of conducting this type of investigation.

5.3. Membrane Morphology and Composition Influence

The uniform distribution of pores (0.8–1.2 μm) examined in SEM analysis exceeds typical values (0.1–0.5 μm) found in zeolites [9], which makes Knudsen diffusion the dominant mechanism since selectivity inversely relates to $\sqrt{(M\_N_2/M\_CO_2)} \approx 0.8$. The observed CO_2/N_2 selectivity value of 1.8 surpassed the Knudsen limit (0.8) at 60°C since Fe_2O_3 facilitated surface diffusion or adsorption-enhanced transport mechanisms [21]. Temperature plays an essential role in surface interactions because this condition decreases adsorption which brings selectivity definition closer to its Knudsen value of 0.7 at 140°C. The membrane transport occurs by means of Knudsen diffusion and surface diffusion simultaneously which supports similar observations made in carbon-based molecular sieve membranes [22] while demonstrating advanced thermal properties. Energy-dispersive spectroscopy scanning confirmed the presence of Fe_2O_3 clusters acting as Lewis acid sites which interact with CO_2's quadrupole moment per study [10]. Future testing under humid multi-component conditions becomes essential to examine how H_2O and SO_2 molecules interfere with the beneficial CO_2-Fe_2O_3 surface interaction which exists at low temperatures [11, 23]. According to Krishna [21] surface diffusion plays an essential role in CO_2 transport within porous ceramics when the temperature falls below 100°C which confirms our experimental results at 60°C. Pore size optimization starting from 0.1–0.5 μm could enhance selectivity by transitioning transport toward molecular sieving at 140°C while reducing permeance according to analysis of Knudsen diffusion prominence [9].

Table 1: Average CO_2 concentration in permeate at various temperatures.

Temperature(C)	CO2 concentration (%) in permeate
60	7.90
80	5.62
100	2.60
140	2.21

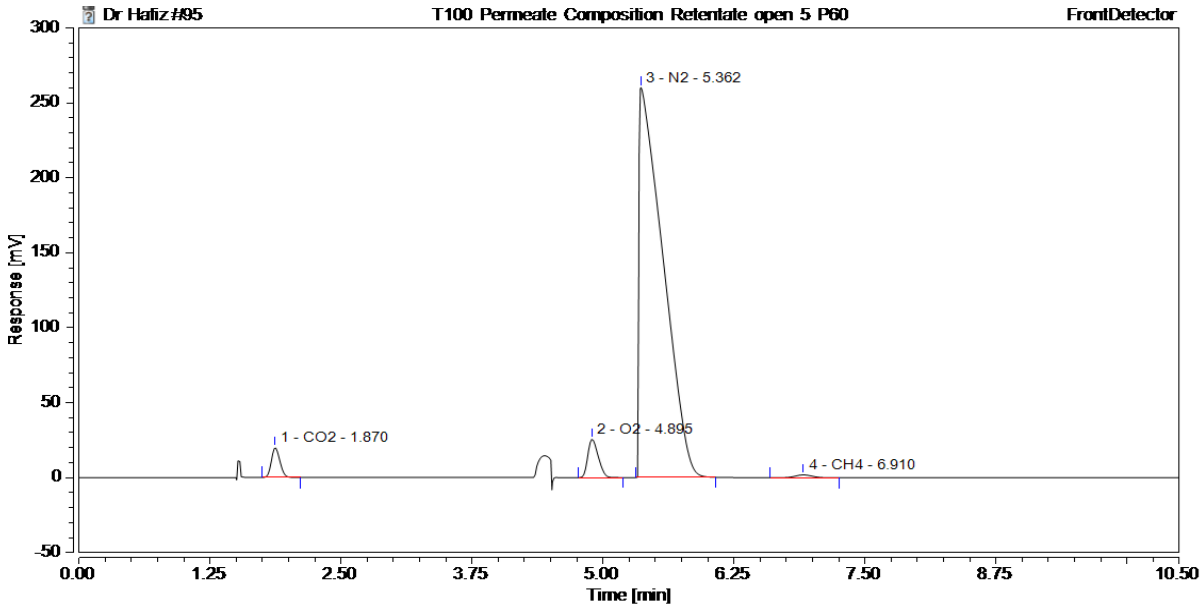

Fig. 4. Gas chromatography results for permeate gas at 60°C and 60 psi.

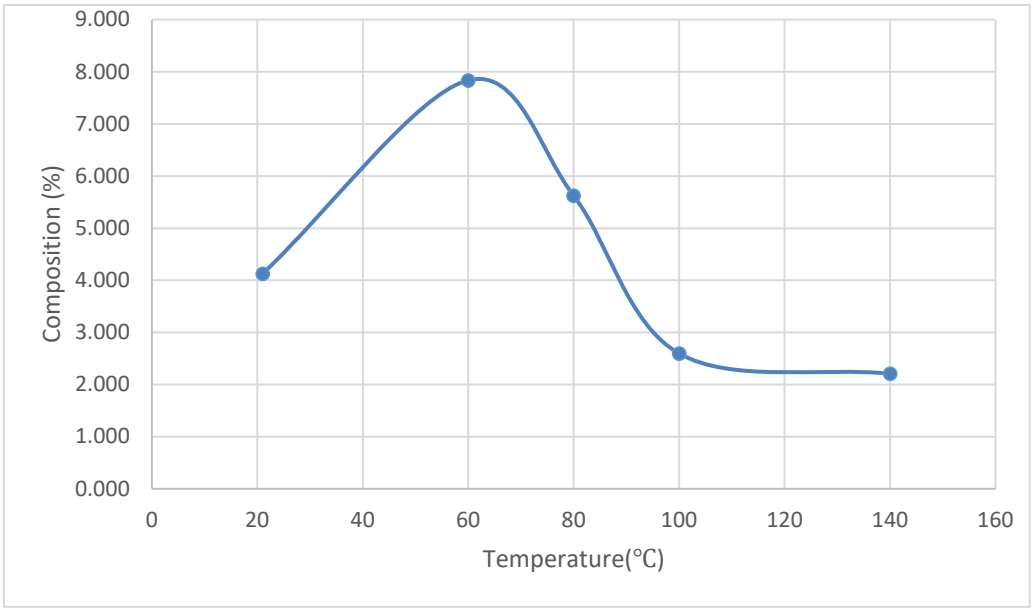

Fig. 5. Red Membrane CO2 Composition vs. Temperature at 40 psi.

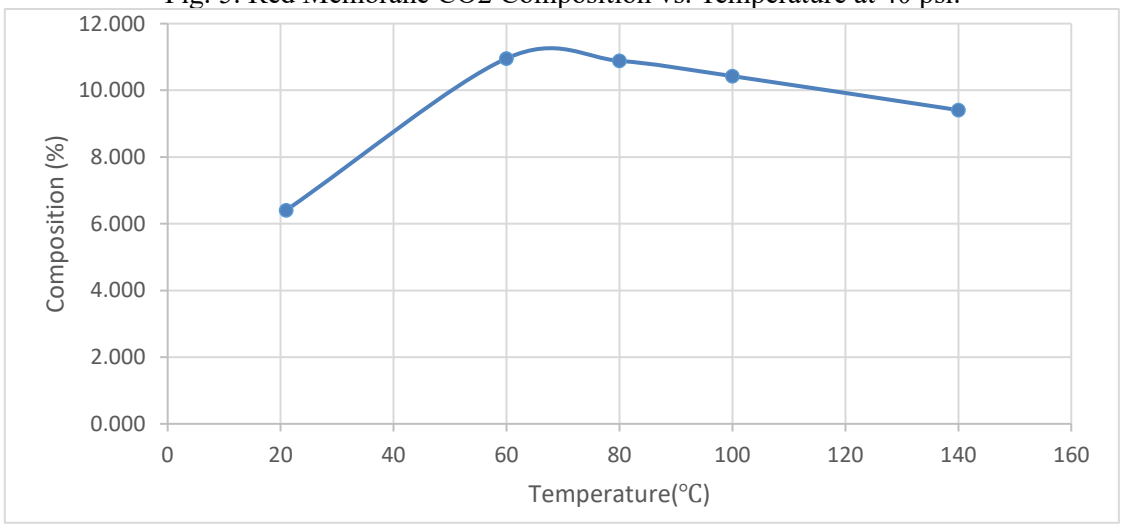

Fig. 6. Red Membrane CO2 Composition vs. Temperature at 80 psi.

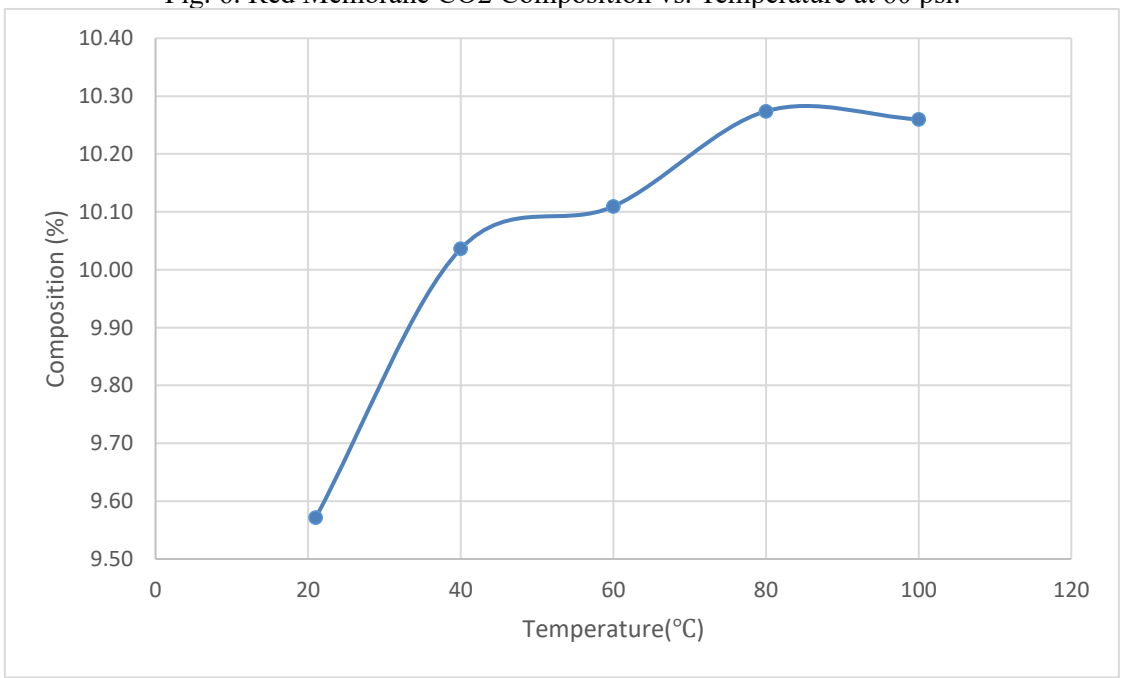

Fig. 7. Red Membrane CO2 Composition vs. Temperature at 80 psi.

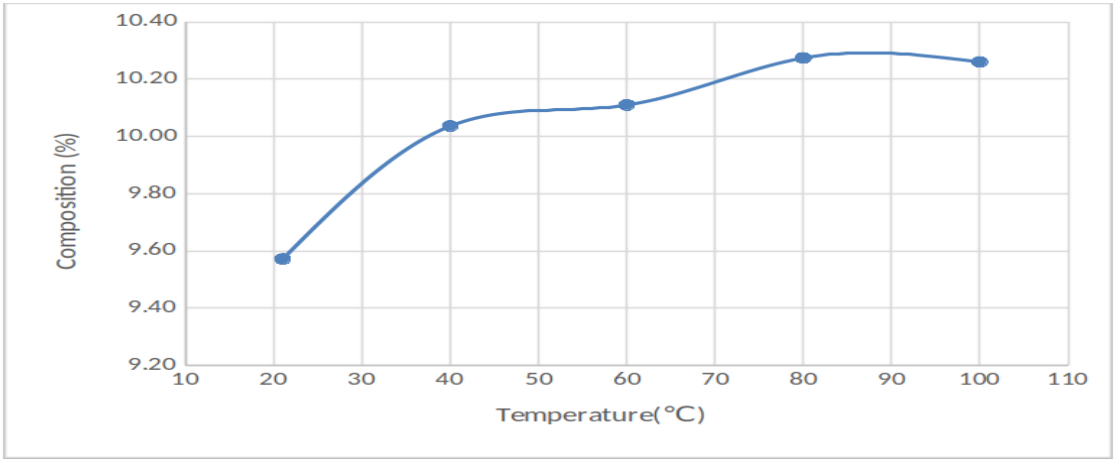

Fig. 8. White Membrane CO2 Composition vs. Temperature at 40 psi.

5.4. ANN Model Performance and Comparative Analysis

The artificial neural network (ANN) process demonstrates its convergence behaviour across 1000 epochs which utilizes multiple performance metrics to display. Figure 9 Presents six Subplots showing separate error and correlation Metrics consisting of (a) Mean Squared Error (MSE) and (b) Mean Absolute Percentage Error (MAPE) along with (c) Mean Squared Logarithmic Error (MSLE) and (d) Log-Cosh Loss and finally (e) Coefficient of Determination (R^2) and (f) Pearson Correlation Coefficient (r). The set of performance metrics serves to determine both the accuracy and predictive reliability of the ANN model for target value prediction.

The progress of training demonstrates improved model performance through decreasing trends in both MSE and MAPE and MSLE and log-cosh loss components. The ANN reaches convergence at 1000 epochs along with MSE = 0.00033 and performance values of MAPE =0.146%, MSLE = 4.1e-06, and log-cosh loss = 0.00016. The model shows excellent generalization ability across the training dataset because of its low error values.

The prediction data matches actual values strongly due to the high values found in goodness-of-fit indicators R^2 and r at 0.998 and 0.997. The ANN model displays high efficiency in data pattern recognition because its near-unity R^2 value demonstrates minimal differences between predicted values and actual outcomes. The high Pearson correlation coefficient (r) along with the predicted and observed values shows a strong linear relationship.

The figure demonstrates the successful combination of ANN model features which shows that the model exhibits reliable predictive functions. The ANN demonstrates reliable performance assessment capabilities because its learning process collects the data distribution effectively which produces decreasing errors and high correlation levels.

The graph in Figure 10 shows the connection between pressure and temperature levels on concentration outcomes by displaying experimental data and ANN model predictions on line and surface plots. The ANN model takes pressure along with temperature as its input data to calculate predicted concentration values. The figure contains three sections including a pressure-specific line plot (a) and temperature-specific line plot (b) alongside a combined surface plot (c) showing both data points and ANN prediction values.

The influence of pressure levels on concentration analysis can be observed in Fig. 10a by comparing experimental results to ANN prediction values using line plots. The ANN successfully generated accurate predictions for the relationship between pressure and concentration measurements. The ANN achieves successful learning of pressure-concentration relationships which leads to minimal differences between actual measurements and predictive outcomes.

Figure 10b presents a line plot from experimental and ANN-predicted materials that investigate the relationship between temperature and concentration. The model demonstrates reliability in predicting temperature-related concentration effects because the experimental and predicted data values show excellent alignment.

The surface plot of Figure 10c displays simultaneous analysis of pressure and temperature's influence on concentration. The experimental data appears as the surface layer whereas the scatter points indicate ANN predicted values. The predicted values of ANN align nicely on the measured experimental results.

The ANN model demonstrates its broad generalization capability based on these dual pressure and temperature variables which indicate its dependable performance in concentration prediction. Overall, Figure 10 highlights the effectiveness of the ANN model in capturing the intricate relationships between pressure, temperature, and concentration.

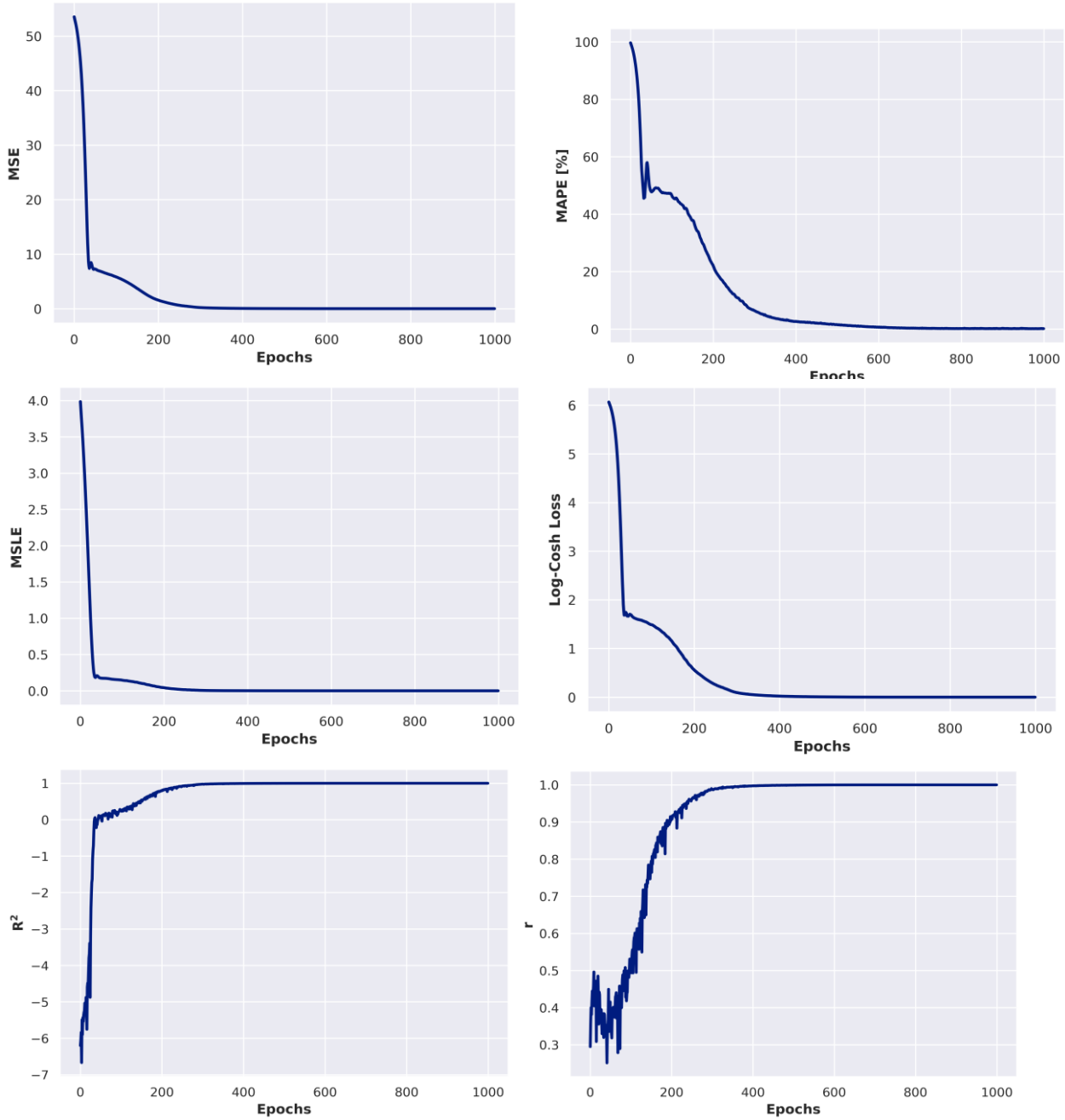

Fig. 9. A convergence of the ANN training data sets for different performance evaluation metrics (a)MSE, (b)MAPE, (c)MSLE, (d)log-cosh loss, (e)R^2 and (f)r.

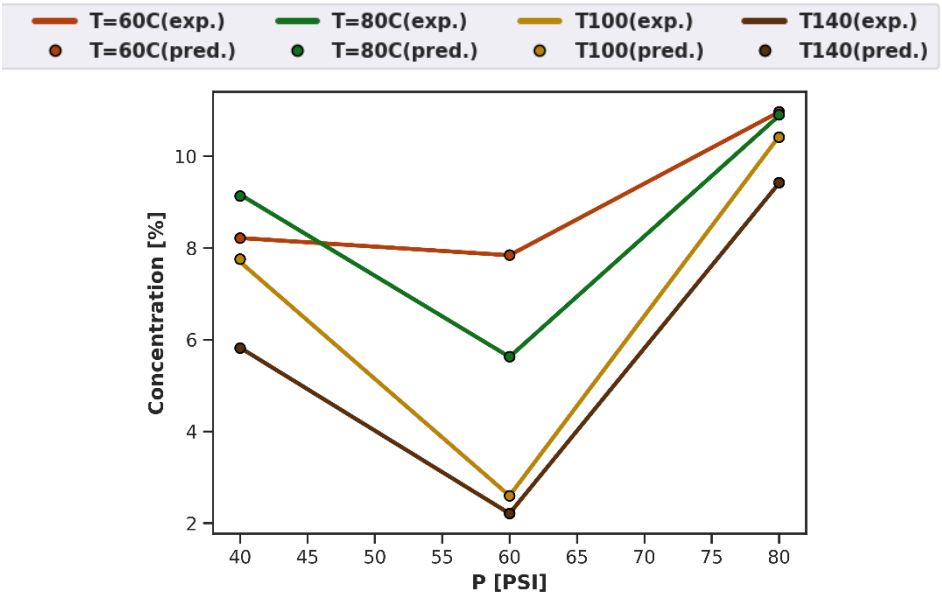

(a)

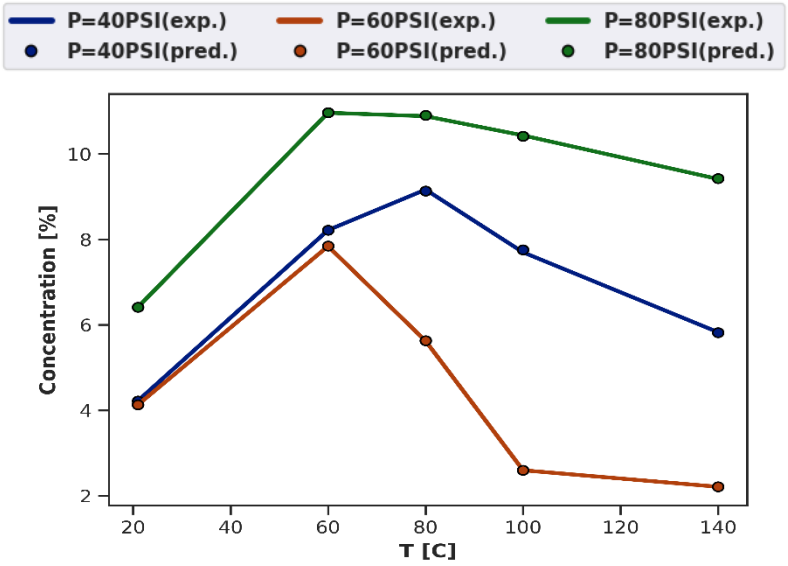

(b)

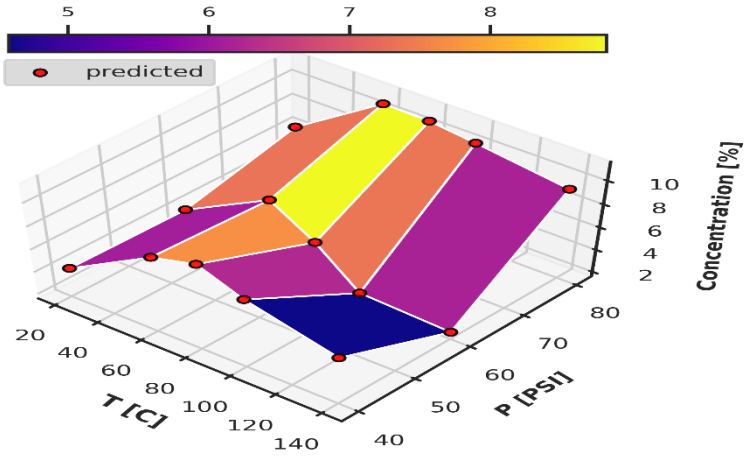

(c)

Fig. 10. Influence of pressure and temperature on concentration, illustrated through line plots (a, b), and surface plots (c) comparing experimental data and ANN predictions.

The strong agreement between experimental measurements and ANN predictions across both line and surface plots validates the model's predictive accuracy and reliability for practical applications.

The experimental concentration data from Figure 11 shows how well the ANN model predicted results when tested at various pressure levels which include (a) 40 PSI, (b) 60 PSI and c) 80 PSI. The subplots show visual verification of ANN model evaluation as they display predicted values relative to experimental results at different pressure levels. The predictive model achieved quantitative assessment through analysis of Mean Squared Error (MSE), Mean Absolute Percentage Error (MAPE), Mean Squared Logarithmic Error (MSLE), Log-Cosh Loss, Coefficient of Determination (R^2) and Pearson Correlation Coefficient (r).

The network model predicts concentrations accurately under P = 40 PSI resulting in 0.0009 MSE and 0.2792% MAPE and 1.2e-05 MSLE and 0.097 log-cosh loss. The model demonstrates strong dependability by showing 0.998 levels of R^2 value and 0.995 Pearson correlation coefficient when compared against experimental values at this particular pressure condition. The graphical representation of the model shows points tightly aligned with the diagonal line indicating its ability to accurately track concentration changes.

The ANN model demonstrates excellent predictive potential at P = 60 PSI according to the data presented in Figure 11(b). The error metrics demonstrate low performance at P = 60 PSI because MSE stands at 0.0008 while MAPE is 0.072% and MSLE is 1.3e-05 and log-cosh loss measures 0.118. Experimental trends produced by the model are validated by an R^2 value of 0.995 and a correlation coefficient (r) of 0.993. The ANN model shows excellent generalization properties because the data points in scatter plots closely follow the diagonal axis.

The ANN model demonstrates excellent performance at P = 80 PSI according to Figure 11(c). The MSE measurement stands at 0.0002 and MAPE stays at 0.1134. A value of 0.094 represents the log-cosh loss as the MSLE registers 2e-06 while displaying an MSE of 0.0002. The predictive and experimental value results demonstrate almost perfect alignment with an R^2 value of 0.996 and a correlation coefficient of 0.998 for a near-linear relationship. Figure 11 shows that the ANN model demonstrates both robustness and accuracy performance when evaluating various pressure conditions in the prediction process. The model demonstrates effective complex pressure-concentration mapping capabilities as shown by its consistent high R^2 and r values together with its minimal error metrics.

The experimental results match well with the predicted values as shown in the scatter plots which proves that ANN performs effectively for predictive analysis across different operational conditions. The performance metrics of the ANN model are displayed in Figure 12 through 3D bar plots which evaluate the regression statistics. The graphical displays comprise three axes where pressure takes the horizontal position and temperature occupies the vertical axis but the selected error or correlation metric stands at the back. Several subfigures show the model assessment results using data from Mean Squared Error (MSE) and Mean Absolute Percentage Error (MAPE) and Mean Squared Logarithmic Error (MSLE) and Log-Cosh Loss and Coefficient of Determination (R^2) and Pearson Correlation Coefficient (r).

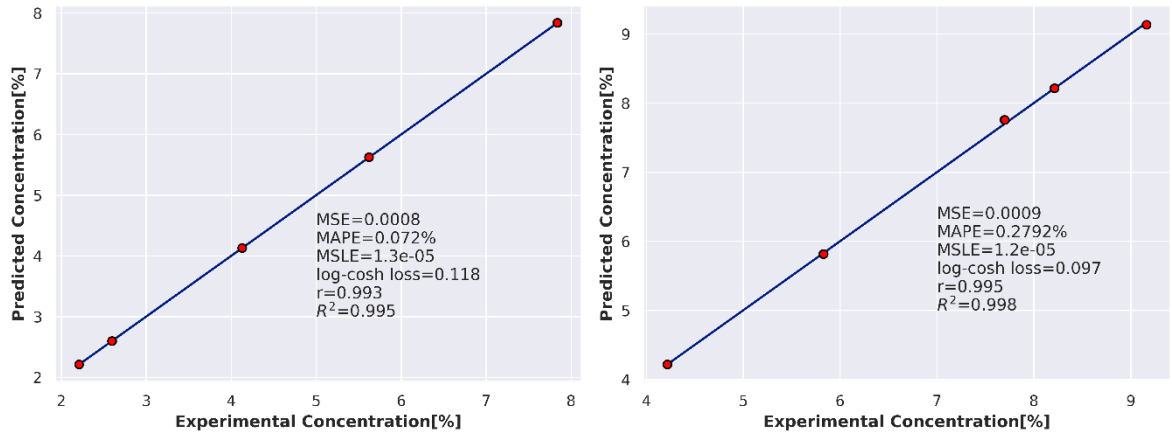

a b

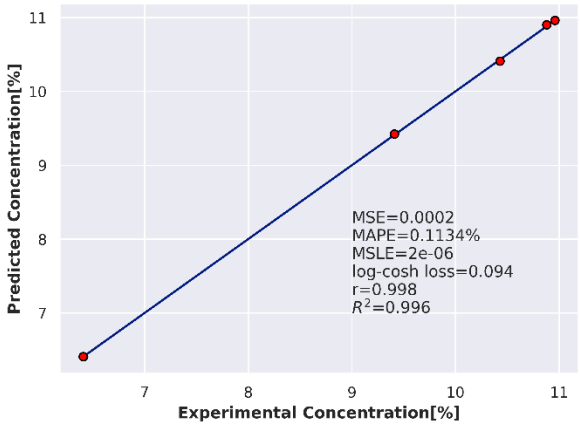

c

Fig. 11. Scatter plots of concentration values from experimental data compared to the corresponding values predicted by the ANN model at (a)P=40PSI, (b)P=60PSI, and (c)P=80PSI

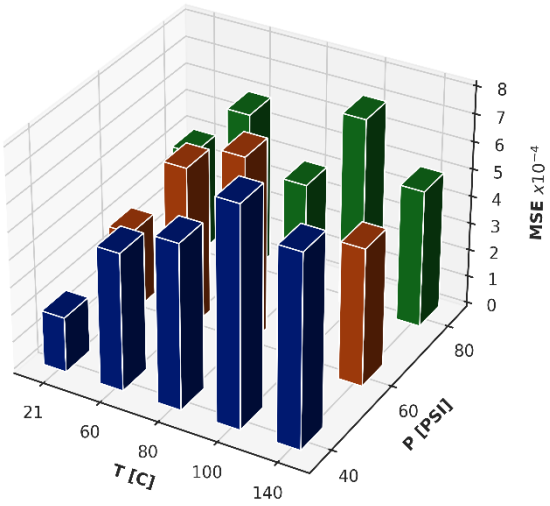

(a)

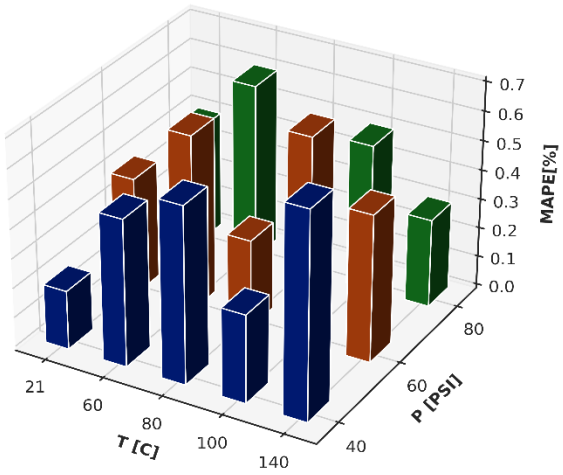

(b)

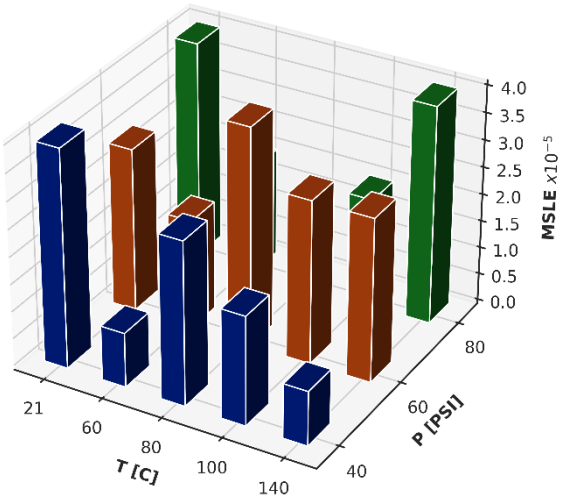

(c)

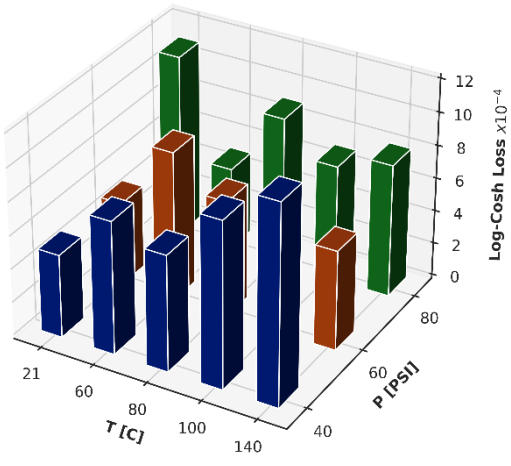

(d)

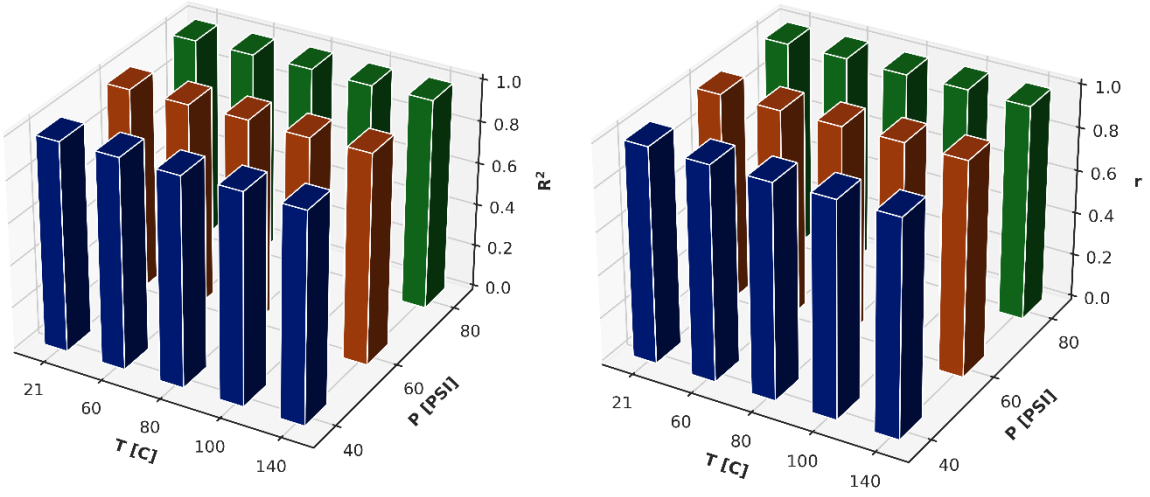

(e) (f)

Fig. 12. Regression statistics of the present ANN model using different performance evaluation metrics (a)MSE, (b)MAPE, (c)MSLE, (d)log-cosh loss, (e)R^2 and (f)r.

The ANN model proves its predictive accuracy and operational versatility through the experimental results. Figure 12(a) shows the MSE distribution across different pressure values, where the highest MSE values recorded is 7e-4 across different operating conditions. These values indicate that the ANN model's predictions align closely with the actual values on average, reflecting strong precision and accuracy. Similarly, Figure 12(b) presents the MAPE values, with maximum errors of 0.7% at 40 PSI, 0.7% at 60 PSI, and 0.6% at 80 PSI. These low percentage errors suggest that the ANN predictions exhibit minimal deviation from the experimental data, confirming the model's high predictive precision. The ANN model demonstrates high predictive capability throughout Figure 12(c) after evaluating data with log-scaled ranges according to MSLE values. Over different operating conditions the model achieves maximum MSLE of 4×10−5. The model demonstrates effective concentration variation prediction capability since its small resulting values show minimal deviation in predictions. The peak values from Figure 12(d) show log-cosh loss standing at 12e-4 when pressure reaches 40 PSI and 9e-4 at 60 PSI and 11e-4 at 80 PSI. This loss function reduces outlier sensitivity leading to superior training results.

The R^2 values in Figure 12(e) exceed 0.99 in each condition thus demonstrating that the model manifests more than 99% variable dependence on the target variable. The model achieves exceptional accuracy by demonstrating R^2 values exceeding 0.99 thus confirming its ability to determine concentration figures through pressure and temperature input. The Pearson correlation coefficient (r) shown in Figure 12(f) maintains a value greater than 0.993 under every pressure situation to indicate a highly dependable linear relationship between experimental and predicted values. The ANNs ability to capture fundamental data patterns stands strong because it provides minimal deviation from experiment levels.

The statistical analysis in Figure 12 demonstrates that ANN provides dependable and accurate predictions regarding the modeled data. The ANN models demonstrate high modeling capacity through its inconsistency in low error metrics and near-unity correlation coefficients and R^2 values for accurately predicting pressure-temperature-concentration relationships. The ANN model shows strong suitability for predictive analysis because it provides dependable exact results in different experimental settings.

5.5. Benchmarking Against Existing Technologies

The selectivity level of MOF-doped ceramics achieves 4–10 but operates within a temperature range lower than 80°C while their production costs are high [17]. Our membrane exhibits a moderate selectivity between 1.8 and 0.7 which makes up for its resistance to heat degradation at 140°C making it suitable for flue gas treatment. The selectivity potential of polymeric membranes reduces at temperatures above 280°C because degradation occurs and plasticization takes effect [8]. The high CO_2/N_2 selectivity (up to 100) of carbon molecular sieve membranes suffers from poor resistance to oxidation as well as limited operational temperatures below 300°C [22].

Our 1000°C heat-stable ceramic membrane serves as a lasting industrial solution for high-temperature applications though it demonstrates lower separation ability indicating a relationship between service duration and operational capabilities.

The operation between 120–140 degrees Celsius eliminates the requirement for flue gas cooling which leads to a 15–20 percent energy reduction compared to amine scrubbing that needs 3.5–4.0 GJ/ton CO_2 for regeneration [15].

When using red clay in fabrication one can reduce manufacturing costs to \$5–10/m² which beats the \$50–100/m² expense for alumina membranes [16]. This improves the economic viability of production. The research by Smart et al. [16] demonstrated that diminishing ceramic membrane expenses could be achieved by selecting local ceramic suppliers which fits our project utilizing Saudi red clay.

5.6. Implications for Industrial Deployment and Future Research

The membrane enables energy-efficient operations at emissions temperatures through its ability to operate without pre-cooling specifically in the situations where flue gas reaches temperatures beyond 120°C in coal-fired plants. Real-time process control becomes possible because the ANNs demonstrate accurate forecasting which enables automatic adjustments to changing pressures and temperatures. Future enhancements to adsorption selectivity at elevated temperatures must include either doping through Fe_2O_3 or MOF incorporation to enhance adsorption sites or using pore sizes below 0.1–0.5 μm for molecular filtration [7, 20, 9]. Tests conducted in conditions with SO_2 and NOx will prove the performance of the system in actual flue gases [11, 23]. The development of planned CFD models will enhance transport predictions through previous research [11, 19].

6. Conclusion

The main goal of this study is the developing and testing of a high temperature CO_2 capturing from flue gas using Saudi red clay based ceramic membranes from local sources in Saudi Arabia, by avoid the need for energy consuming cooling process from the conventional amine based capturing systems while keeping effective separation at high operating temperatures. An ANN model is developed to estimate the membrane performance (CO2 concentration (%) in permeate) using results obtained from the present experimental results and utilizing pressure and temperature as ANN input parameters. The ANN model exhibited highly accurate predictions, as evidenced by the extremely low values of MSE, MAPE, MSLE, and log-cosh loss metrics, along with exceptionally high values of the R^2 and Pearson correlation coefficients. The research led to several significant findings, outlined as follows.

- Fe_2O_3 rich ceramic membranes from this raw material enabled a stable operation at temperatures up to 140°C under 40 to 80 psi pressures with separation efficiency 7.9% CO_2 at 60°C and 60 psi pressure.
- The structure of the applied membrane maintained their efficiency during heating compared to both polymeric systems that failed below 280°C alongside MOF-ceramic membranes which may lose its efficiency over 80 °C.
- The red clay membrane technology demonstrates practical production value because it combines high-temperature resistance (above 1000°C), cost-effectiveness (between \$5 to \$10 per square meter) with acceptable separation performance (CO_2/N_2 ratio between 1.8 and 0.7). This makes it suitable for industrial flue gas integration. This technical approach eliminates pre-cooling requirements that decrease energy consumption levels between 15-20% to resolve the main issue with amine scrubbing.
- The ANN model exhibited strong convergence behavior over 1000 training epochs, with a significant reduction in prediction error.
- The final performance metrics (MSE = 0.00033, MAPE = 0.146%, MSLE = 4.1×10^{-6}, log-cosh loss = 0.00016) indicate that the model generalizes well across the training dataset.
- The goodness-of-fit measures ($R^2 = 0.998$, $r = 0.997$) confirm a strong linear correlation between predicted and actual values.
- Across different pressure conditions, the ANN model maintained high predictive precision, with maximum values of MSE, MAPE, MSLE and log-cosh loss equal values of 7e-4, 0.7%, 4×10^{-5} and 12e-4 respectively.
- The ANN model successfully captured complex relationships between temperature, pressure, and CO_2 separation, demonstrating its potential for industrial applications in process optimization and control.

Overall, this study highlights the effectiveness of ANN-based modeling in predicting CO_2 separation performance with high accuracy and reliability. Future work could focus on expanding the model to incorporate additional operational parameters and further optimizing its architecture to enhance predictive performance.

Funding
This project was funded by the National Plan for Science Technology and Innovation (MAARIFAH)—King Abdulaziz City for Science and Technology—the Kingdom of Saudi Arabia, Project number 11-ENV1786-08.

References

1. IEA. Global Energy Review: CO_2 Emissions in 2023. International Energy Agency, 2024.
2. Leung, D. Y. C.; Caramanna, G.; Maroto-Valer, M. M. An overview of current status of carbon dioxide capture and storage technologies. Renewable and Sustainable Energy Reviews 2014, 39, 426–443.
3. Rochelle, G. T. Amine Scrubbing for CO_2 Capture. Science 2009, 325, 1652–1654.
4. Gude, V.; et al. Ceramic Membranes for High-Temperature Gas Separation. Energy & Fuels 2018, 32, 963–970.
5. Rahman, M. H.; et al. Sustainable Ceramic Membranes from Saudi Red Clay for CO_2 Capture. Journal of Environmental Chemical Engineering 2023, 11, 109456.
6. Baker, R. W. Membrane Technology and Applications, 3rd ed.; John Wiley & Sons, 2012.
7. Li, H.; et al. High-Performance Ceramic Membranes for CO_2 Separation. Journal of Membrane Science 2020, 601, 117789.
8. Sanders, D. F. ; et al. Plasticization in Polymeric Membranes for Gas Separation. Polymer 2013, 54, 4729–4761.
9. Sholl, D. S.; Johnson, J. K. Making High-Flux Membranes with Poly(amide-imide)s. Science 2006, 312, 1003–1004.
10. Yang, R. T. Adsorbents: Fundamentals and Applications; John Wiley & Sons, 2003.
11. Ribeiro, A. M.; et al. CO_2 Capture by Adsorption: A Review. Chemical Engineering Journal 2018, 332, 355–366.
12. Freeman, B. D. Basis of Permeability/Selectivity Tradeoff Relations in Polymeric Gas Separation Membranes. Macromolecules 1999, 32, 375–380.
13. Zhang, Y.; et al. Ceramic Membranes for CO_2 Separation: A Review. Industrial & Engineering Chemistry Research 2019, 58, 6536–6545.
14. Sema, T.; et al. Artificial Neural Network Modeling of CO_2 Capture Process. International Journal of Greenhouse Gas Control 2021, 109, 103383.
15. IPCC. Special Report on Carbon Dioxide Capture and Storage; Cambridge University Press, 2005.
16. Smart, S.; et al. Cost-Effective Ceramic Membranes for Gas Separation. Ceramics International 2015, 41, 950–960.
17. Zhang, C.; et al. Metal-Organic Framework-Based Membranes for CO_2 Separation. Advanced Materials 2018, 30, 1705482.
18. Chen, J.; et al. High-Temperature Stability of Ceramic Membranes for Gas Separation. Separation and Purification Technology 2019, 210, 456–465.
19. Ahmad, A. L. ; et al. Computational Fluid Dynamics Modeling of Gas Separation in Ceramic Membranes. Computers & Chemical Engineering 2017, 102, 45–56.
20. Yang, S.; et al. Fe_2O_3-Doped Ceramic Membranes for Enhanced CO_2 Adsorption. Journal of Materials Chemistry A 2019, 7, 1201–1210.
21. Krishna, R. Diffusion in Porous Crystalline Materials. The Journal of Physical Chemistry C 2009, 113, 19756–19781.
22. Koros, W. J.; et al. Carbon Molecular Sieve Membranes for Gas Separation. Journal of Membrane Science 2017, 533, 1–10.
23. Wang, L.; et al. Zeolite Membranes for CO_2 Separation under Humid Conditions. Microporous and Mesoporous Materials 2020, 301, 110234.